Available online at www.sciencedirect.com
ScienceDirect
Journal of Sound and Vibration 315 (2008) 1016–1034
JOURNAL OF SOUND AND VIBRATION
www.elsevier.com/locate/jsvi

Investigation of the influence of liner hard-splices on duct radiation/propagation and mode scattering

Bing Yang, T.Q. Wang*

Department of Fluid Machinery, School of Jet Propulsion, Beijing University of Aeronautics and Astronautics, Beijing, China

Received 1 March 2006; received in revised form 2 February 2008; accepted 10 February 2008
Handling editor: L.G. Tham
Available online 2 April 2008

Abstract

In a turbofan engine, usually, the acoustically lined region consists of several liner segments separated by longitudinal hard-splices due to manufacturing. The non-uniform impedance in the circumferential direction will excite other circumferential modes besides the incident modes. Consequently, the acoustic propagation in and radiation from a turbofan is considerably different from that of an uniform impedance. To investigate the effect of liner hard-splices on acoustic radiation and propagation, a boundary integral equation method (BIEM) in two-dimensional (2D) is expanded into a three-dimensional form. In this model, an axially uniform inflow passes a cylindrical finite duct and the liner inside the duct may be circumferentially or axially non-uniform. The verifications are presented and the influence of hard-splices is investigated. Then an infinite duct model is developed to investigate the mechanism of mode scattering excited by a circumferentially non-uniform boundary. BIEM is combined with the mode-matching method. The model is validated by comparing with the analytical result in an infinite circular duct with a hard wall. Then a variety of liner configurations containing periodic/non-periodic hard-splices are studied and the mode scattering mechanism is discussed.
© 2008 Elsevier Ltd. All rights reserved.

1. Introduction

The ducted-fan tone noise generated by modern high-bypass-ratio turbofan aero-engines operating at supersonic fan tip speeds has become one of the principal aircraft engine noise sources. The prediction of ducted-fan noises is one of the key elements affecting the design of new engines. In the last few decades, although considerable success has been achieved in understanding and optimizing the attenuation of sound waves in an acoustically lined duct, there still remain various areas that require more attention and further investigations. In particular, the effect of circumferentially non-uniform impedance on the acoustic propagation in and radiation from a duct has received relatively little attention.

Acoustic liners are often assumed to be circumferentially uniform in the design stage; then the acoustic field of a duct is axisymmetric. Actually, due to the restriction of manufacturing capacity, the acoustic liners in nacelle have hard-splices in the circumferential direction, which separate adjacent liner panels, shown in Fig. 1.

*Corresponding author. Tel./fax: +86 10 82317407.
E-mail address: wangtq@buaa.edu.cn (T.Q. Wang).

0022-460X/$ - see front matter © 2008 Elsevier Ltd. All rights reserved.
doi:10.1016/j.jsv.2008.02.010

Nomenclature

a	duct radius
$A^{\pm}_{m_0n_0}$	complex modal coefficients
B	number of spinning points
c	sound velocity
$E_{m_0n_0}$	eigenfunction in duct acoustics
$E^{*}_{m_0n_0}$	conjugate of $E_{m_0n_0}$
f_1	interior surface of the duct wall
f_2	interior surface of the duct upstream opening
f_3	interior surface of the duct downstream opening
f_4	exterior surface of the duct wall
f_5	exterior surface of the duct upstream opening
f_6	exterior surface of the duct downstream opening
F_T	thrust of each spinning point
G_{3-H}	Green function of a 3D Helmholtz equation
J	Bessel function; number of hard-splices
k	wavenumber
ka	Helmholtz number
k_{r,m_0n_0}	radial wavenumber in duct acoustics
$k^{\pm}_Z$	axial wavenumber in duct acoustics
l	arbitrary integer
L	duct length
m_0	circumferential mode order
m_I	circumferential mode order of an excited mode
M	maximal circumferential modal order
Ma	V/c Mach number of a moving duct
n_0	radial mode order
N	maximal radial modal order
p'	acoustic pressure
Q	coefficient of acoustic pressure
(r, θ, z)	reference frame fixed in fluid at rest
(r, θ, Z)	moving stretched frame of reference
r'_0	radius of spinning points
V	velocity of duct moving
$\mathbf{x}_j$, $\mathbf{X}$	observer point
$\mathbf{y}_j$, $\mathbf{Y}$	source point
zn	specific acoustic impedance
Ω	rotating velocity of the fan axis
β	$\sqrt{1-Ma^2}$
κ	k/β

The liners' performance will be affected by these liner hard-splices and this is verified by experimental investigations. The in-flight measurements of circumferential modal spectra of the Rolls-Royce Tay 650 engine installed on the Fokker 100 aircraft indicated that the acoustic radiation from the inlet was substantially affected by the presence of hard-splices [1]. In addition, these measurements confirmed that the same engine radiated a substantially lower noise level when fitted with a single-piece liner as opposed to a three-splice liner. Other experimental studies [2] have corroborated these findings. The acoustic circumferential mode transmitting inside a duct can be transferred from an incident mode to some others by this circumferentially non-uniform acoustic property, which is different from that of a uniform liner. An experimental program in the NLR spinning mode synthesizer was carried out to study the modulation effect caused by hard-splices [2].

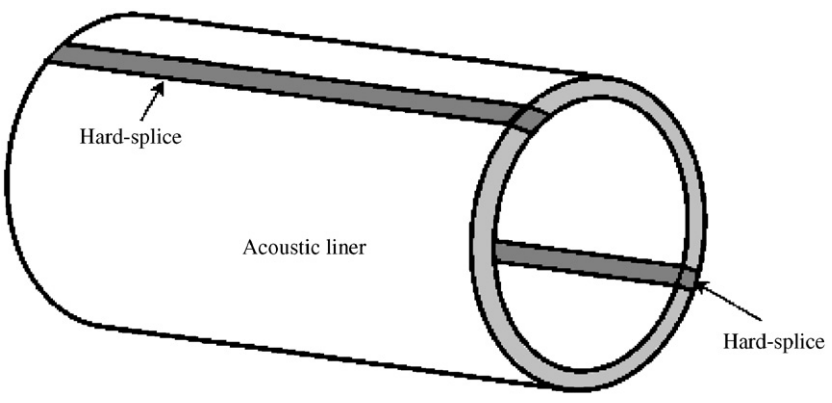

Fig. 1. Sketch of an acoustic liner with longitudinal hard-splices.

It is now evident that it is desirable to estimate the influence of hard-splices on the behavior of acoustic liners. Therefore, the development of tools to determine this influence is important.

Due to the non-uniform impedance boundary caused by hard-splices on liners, three-dimensional (3D) calculations are required. Many computational approaches such as FEM [3,4], and CAA [5–7] have been applied for the non-uniform impedance boundary. Complex actual duct geometries and flows can be dealt with by these approaches, but the excessive computational time and memory requirements are expensive against these advantages, which make it impractical for direct application to parametric or liner optimization designs studies. Another numerical method called the point-matching method has also been used to analyze the problem of hard-splices on liners [8]. The ability to compute any portion of the sound field without calculating the entire field makes its calculation faster than that by FEM and CAA methods. It is unfortunate that in this model the flow is neglected and a finite duct is not involved. Analytical methods are accurate and rapid for prediction when the duct geometries and the flows are simple. But the complex eigenequations in analytical methods are difficult to solve [9,10] and the radiation from a finite duct will not be dealt with in these analytical methods.

In the numerical methods mentioned above, the investigation focuses only on the upstream propagation inside a duct. In the analytical methods, the acoustic reflections at the duct openings are neglected, viz. the duct is semi-infinite. Neither the acoustic interferences by the acoustic pressure radiated from the upstream/downstream openings nor the acoustic reflections from both openings are considered in these models. These interferences and reflections are important since present-day wide-cord-fan engine ducts have a length-to-diameter ratio $L/D<1$ and it is obvious that the interferences from both duct openings cannot be neglected due to the short length of the duct and the high frequencies of the acoustic sources. Furthermore, the incident sources in all the above models must be specific modal coefficients, which are not easy to obtain in practice.

In this paper a 3D boundary element model in the frequency domain has been developed to deal with a circumferentially non-uniform impedance boundary. The acoustic field inside/outside a duct is obtained simultaneously by this model, involving the upstream/downstream acoustic propagation inside a finite duct and the reflection/radiation from both the openings. This model has been verified [11] by predicting the acoustic directivities of a finite duct with a circumferentially uniform boundary. In this paper the interior surface of a duct wall may have arbitrarily distributed locally reacting liners, circumferentially segmented or axially segmented. The incident sources are inside the duct and assumed to be known in advance, which can be easily obtained. An infinite duct model by boundary integral equation method (BIEM) combined with the mode-matching method has also been developed to study the mode scattering phenomena caused by liner hard-splices.

The aim of our work is to investigate the effects of hard-splices and to compare the performance of circumferentially segmented liners with that of uniform liners, and furthermore, to investigate the mode scattering phenomena caused by hard-splices. For engineering purposes, an accurate and rapid method is presented in this paper to evaluate the hard-splices' scattering effects on noise reductions.

2. Finite length duct model by BIEM

2.1. Physical model and boundary integral equations

It is assumed that a turbofan duct is modeled approximately by a cylindrical duct containing an axially uniform mean-flow. All the nonlinear effects are neglected. The total acoustic field is partitioned into two regions: the acoustic propagation inside the duct and the acoustic radiation outside the duct. The boundary surfaces of the propagation are composed of the interior wall of the duct denoted by f_1, the interior surface of the duct upstream opening and the downstream opening denoted by f_2, f_3. The boundary surfaces of the radiation are composed of the exterior wall of the duct denoted by f_4 and the exterior surface of the duct upstream opening and the downstream opening denoted by f_5, f_6. All the boundary surfaces of a finite duct are shown in Fig. 2.

The total acoustic pressure propagated inside the duct is a sum of the known incident acoustic pressure and the unknown scattering acoustic pressure

$$p'_t = p'_i + p'_s. \tag{1}$$

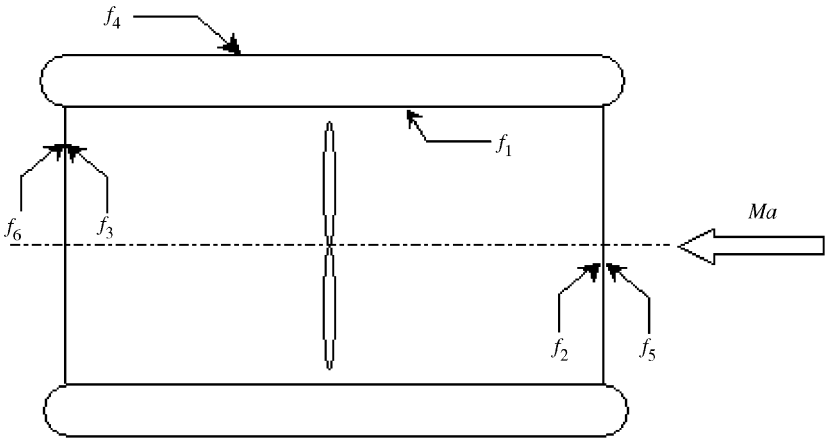

Fig. 2. Sketch of finite duct boundary surfaces.

In the outer region there exists no incident sound pressure except for the scattering pressure

$$p'_t = p'_s. \tag{2}$$

A uniform axial inflow with Mach number Ma passes the duct, namely the medium is at rest and the duct is moving in the axial direction with Mach number Ma. In a frame of fluid at rest (r,θ,z), p'_s in the regions barring duct surfaces is governed by a homogeneous wave equation in cylindrical coordinate as follows:

$$\left[\frac{1}{c^2}\frac{\partial^2}{\partial t^2} - \frac{1}{r}\frac{\partial}{\partial r}\left(r\frac{\partial}{\partial r}\right) - \frac{1}{r^2}\frac{\partial^2}{\partial \theta^2} - \frac{\partial^2}{\partial z^2}\right]p'_s = 0. \tag{3}$$

The acoustic pressure is periodic in an axially moving and stretched frame with $Z = (z - Vt)/\beta$; the Fourier form is

$$p'_s(r,\theta,Z,t) = \sum_{n=-\infty}^{\infty} Q_s^n(r,\theta,Z)\mathrm{e}^{\mathrm{i}(nB\Omega t - \kappa MaZ)}. \tag{4}$$

Translating into the moving and stretched frame and moving time dependence the governing Eq. (3) is converted into a 3D Helmholtz equation

$$\left[\frac{1}{r}\frac{\partial}{\partial r}\left(r\frac{\partial}{\partial r}\right) + \frac{\partial^2}{\partial Z^2} + \frac{1}{r^2}\frac{\partial^2}{\partial \theta^2} + \kappa^2\right]Q_s^n(r,\theta,Z) = 0. \tag{5}$$

The detailed derivation from Eq. (3) to Eq. (5) can be found in Appendix A of Ref. [11].

The Green function of a 3D Helmholtz equation is

$$G_{3-H}(\mathbf{Y}|\mathbf{X}) = \frac{\mathrm{e}^{-\mathrm{i}\kappa R}}{4\pi R}, \tag{6}$$

where

$$R = \sqrt{r^2 + r'^2 - 2rr'\cos(\theta - \theta') + (Z - Z')^2}. \tag{7}$$

Here (r, θ, Z) is the coordinate of the observer point $\mathbf{X}$ which refers to a point inside or outside the duct. (r', θ, Z') is the coordinate of the source point $\mathbf{Y}$ which refers to a point on the interior/exterior surfaces of the duct. Then the solution of Eq. (5) can be expressed in a boundary integral equation form

$$Q_s^n(\mathbf{X}) = \int_S \left[Q^n(\mathbf{Y})\frac{\partial G_{3-H}(\mathbf{Y}|\mathbf{X})}{\partial n} - G_{3-H}(\mathbf{Y}|\mathbf{X})\frac{\partial Q^n(Y)}{\partial n}\right]\mathrm{d}S. \tag{8}$$

The integral surfaces are the interior/exterior surfaces of the duct wall and duct openings. The normal direction of a boundary is pointed toward the regions, so that the normal direction of the interior duct surfaces is opposite to that of the exterior surfaces. The incident acoustic pressure and the total acoustic pressure can also be written as

$$p_i'(r,\theta,Z,t)=\sum_{n=-\infty}^{\infty} Q_i^n(r,\theta,Z)\,\mathrm{e}^{\mathrm{i}(nB\Omega t-\kappa MaZ)}, \tag{9}$$

$$p_t'(r,\theta,Z,t)=\sum_{n=-\infty}^{\infty} Q_t^n(r,\theta,Z)\,\mathrm{e}^{\mathrm{i}(nB\Omega t-\kappa MaZ)}. \tag{10}$$

According to Eq. (1) the coefficient $Q_t{}^n$ of the total interior acoustic pressure is governed by

$$Q_t^n(\mathbf{X})=\int_S\left[Q_t^n(\mathbf{Y})\frac{\partial G_{3-H}(\mathbf{Y}|\mathbf{X})}{\partial n}-G_{3-H}(\mathbf{Y}|\mathbf{X})\frac{\partial Q_t^n(Y)}{\partial n}\right]\mathrm{d}S+Q_i^n(\mathbf{X}). \tag{11}$$

The integral surfaces are composed of f_1, f_2 and f_3. The coefficient $Q_{t\psi}{}^n$ of the external acoustic pressure is governed by

$$Q_t^n(\mathbf{X})=\int_S\left[Q_t^n(\mathbf{Y})\frac{\partial G_{3-H}(\mathbf{Y}|\mathbf{X})}{\partial n}-G_{3-H}(\mathbf{Y}|\mathbf{X})\frac{\partial Q_t^n(\mathbf{Y})}{\partial n}\right]\mathrm{d}S. \tag{12}$$

The integral surfaces are composed of f_4, f_5 and f_6.

If $Q_t{}^n(\mathbf{Y})$ on the integral surfaces is known, the $Q_t{}^n(\mathbf{X})$ at any point could be obtained by Eqs. (11) and (12). When the observer points are located on the integral surfaces a coupling equation can be obtained. The coefficient $Q_{t\psi}{}^n$ of the acoustic pressure on the smooth interior surfaces is governed by

$$\frac{1}{2}Q_t^n(\mathbf{X})=\int_S\left[Q_t^n(\mathbf{Y})\frac{\partial G_{3-H}(\mathbf{Y}|\mathbf{X})}{\partial n}-G_{3-H}(\mathbf{Y}|\mathbf{X})\frac{\partial Q_t^n(\mathbf{Y})}{\partial n}\right]\mathrm{d}S+Q_i^n(\mathbf{Y}). \tag{13}$$

The coefficient $Q_{t\psi}{}^n$ of the acoustic pressure on the smooth exterior surfaces is governed by

$$\frac{1}{2}Q_t^n(\mathbf{X})=\int_S\left[Q_t^n(\mathbf{Y})\frac{\partial G_{3-H}(\mathbf{Y}|\mathbf{X})}{\partial n}-G_{3-H}(\mathbf{Y}|\mathbf{X})\frac{\partial Q_t^n(\mathbf{Y})}{\partial n}\right]\mathrm{d}S. \tag{14}$$

The impedance boundary condition on the interior surface of a duct wall is [11]

$$\frac{\partial Q_t^n}{\partial n}=-\frac{\mathrm{i}Ma^2}{\beta^3 zn\kappa}\left(\frac{\partial^2 Q_t^n}{\partial Z^2}-\frac{2\mathrm{i}\kappa}{Ma}\frac{\partial Q_t^n}{\partial Z}-\frac{\kappa^2}{Ma^2}Q_t^n\right). \tag{15}$$

The boundary condition of a rigid wall is

$$\frac{\partial Q_t^n}{\partial n}=0. \tag{16}$$

The specific impedance zn is normalized with respect to the characteristic impedance $\rho_0 c_0$ of the air. From Eqs. (13) and (15), the governing equation of $Q_t{}^n$ on the interior surfaces of the wall and upstream/downstream openings can be written as

$$\begin{aligned}\frac{1}{2}Q_t^n(\mathbf{X})=&\int_{f_1}\left[Q_t^n(\mathbf{Y})\frac{\mathrm{e}^{-\mathrm{i}\kappa R}(\mathrm{i}\kappa R+1)}{4\pi R^2}\frac{(r'-r\cos(\theta-\theta'))}{R}\right]\mathrm{d}S\\&+\int_{f_1}\left[\frac{\mathrm{i}Ma^2\mathrm{e}^{-\mathrm{i}\kappa R}}{4\pi R\beta^2 znk}\left(\frac{\partial^2 Q_t^n(Y)}{\partial Z^2}-\frac{2\mathrm{i}k}{\beta Ma}\frac{\partial Q_t^n(Y)}{\partial Z}-\frac{k^2}{\beta^2 Ma^2}Q_t^n(\mathbf{Y})\right)\right]\mathrm{d}S\\&+\int_{f_2}\left[Q_t^n(\mathbf{Y})\frac{\mathrm{e}^{-\mathrm{i}\kappa R}(\mathrm{i}\kappa R+1)}{4\pi R^2}\frac{(Z'-Z)}{R}+\frac{\partial Q_t^n(Y)}{\partial Z}\frac{\mathrm{e}^{-\mathrm{i}\kappa R}}{4\pi R}\right]\mathrm{d}S\\&+\int_{f_3}\left[-Q_t^n(\mathbf{Y})\frac{\mathrm{e}^{-\mathrm{i}\kappa R}(\mathrm{i}\kappa R+1)}{4\pi R^2}\frac{(Z'-Z)}{R}-\frac{\partial Q_t^n(Y)}{\partial Z}\frac{\mathrm{e}^{-\mathrm{i}\kappa R}}{4\pi R}\right]\mathrm{d}S+Q_i^n(\mathbf{Y}).\end{aligned} \tag{17}$$

The partial differential terms $\partial^2 Q_t^n/\partial Z^2$ and $\partial Q_t^n/\partial Z$ on the interior wall f_1 in Eq. (17) can be expressed by the differential schemes about Q_t^n. If the surface f_1 is rigid, Eq. (17) reduces to

$$\begin{aligned}\frac{1}{2}Q_t^n(\mathbf{X}) = &\int_{f_1} Q_t^n(\mathbf{Y})\frac{e^{-i\kappa R}(i\kappa R+1)}{4\pi R^2}\frac{(r'-r\cos(\theta-\theta'))}{R}\,dS\\ &+\int_{f_2}\left[Q_t^n(\mathbf{Y})\frac{e^{-i\kappa R}(i\kappa R+1)}{4\pi R^2}\frac{(Z'-Z)}{R}+\frac{\partial Q_t^n(\mathbf{Y})}{\partial Z}\frac{e^{-i\kappa R}}{4\pi R}\right]dS\\ &+\int_{f_3}\left[-Q_t^n(\mathbf{Y})\frac{e^{-i\kappa R}(i\kappa R+1)}{4\pi R^2}\frac{(Z'-Z)}{R}-\frac{\partial Q_t^n(\mathbf{Y})}{\partial Z}\frac{e^{-i\kappa R}}{4\pi R}\right]dS+Q_i^n(\mathbf{Y}).\end{aligned} \tag{18}$$

If the exterior wall of the duct f_4 is rigid, the governing equation of Q_t^n on the exterior surfaces of the duct wall and upstream/downstream openings is

$$\begin{aligned}\frac{1}{2}Q_t^n(\mathbf{X}) = &\int_{f_4}\left[-Q_t^n(\mathbf{Y})\frac{e^{-i\kappa R}(i\kappa R+1)}{4\pi R^2}\frac{(r'-r\cos(\theta-\theta'))}{R}\right]dS\\ &+\int_{f_5}\left[-Q_t^n(\mathbf{Y})\frac{e^{-i\kappa R}(i\kappa R+1)}{4\pi R^2}\frac{(Z'-Z)}{R}-\frac{\partial Q_t^n(Y)}{\partial Z}\frac{e^{-i\kappa R}}{4\pi R}\right]dS\\ &+\int_{f_6}\left[Q_t^n(\mathbf{Y})\frac{e^{-i\kappa R}(i\kappa R+1)}{4\pi R^2}\frac{(Z'-Z)}{R}+\frac{\partial Q_t^n(Y)}{\partial Z}\frac{e^{-i\kappa R}}{4\pi R}\right]dS.\end{aligned} \tag{19}$$

Continuous conditions are used on the upstream/downstream openings

$$Q_{t(f_2)}^n = Q_{t(f_5)}^n, \quad Q_{t(f_3)}^n = Q_{t(f_6)}^n, \tag{20a,b}$$

$$\frac{\partial Q_{t(f_2)}^n}{\partial Z} = \frac{\partial Q_{t(f_5)}^n}{\partial Z}, \quad \frac{\partial Q_{t(f_3)}^n}{\partial Z} = \frac{\partial Q_{t(f_6)}^n}{\partial Z}. \tag{21a,b}$$

When Q_t^n on all the integral surfaces are obtained by Eqs. (17)–(21), the acoustic pressure of any portion of interest in the acoustic field can be expressed. For any observer point $\mathbf{X}$ inside the duct

$$\begin{aligned}Q_t^n(\mathbf{X}) = &\int_{f_1}\left[Q_t^n(\mathbf{Y})\frac{e^{-i\kappa R}(i\kappa R+1)}{4\pi R^2}\frac{(r'-r\cos(\theta-\theta'))}{R}\right]dS\\ &+\int_{f_1}\left[\frac{iMa^2e^{-i\kappa R}}{4\pi R\beta^2 znk}\left(\frac{\partial^2 Q_t^n(\mathbf{Y})}{\partial Z^2}-\frac{2ik}{\beta Ma}\frac{\partial Q_t^n(\mathbf{Y})}{\partial Z}-\frac{k^2}{\beta^2 Ma^2}Q_t^n(\mathbf{Y})\right)\right]dS\\ &+\int_{f_2}\left[Q_t^n(\mathbf{Y})\frac{e^{-i\kappa R}(i\kappa R+1)}{4\pi R^2}\frac{(Z'-Z)}{R}+\frac{\partial Q_t^n(\mathbf{Y})}{\partial Z}\frac{e^{-i\kappa R}}{4\pi R}\right]dS\\ &+\int_{f_3}\left[-Q_t^n(\mathbf{Y})\frac{e^{-i\kappa R}(i\kappa R+1)}{4\pi R^2}\frac{(Z'-Z)}{R}-\frac{\partial Q_t^n(\mathbf{Y})}{\partial Z}\frac{e^{-i\kappa R}}{4\pi R}\right]dS+Q_i^n(\mathbf{X}).\end{aligned} \tag{22}$$

For any observer point $\mathbf{X}$ outside the duct

$$\begin{aligned}Q_t^n(\mathbf{X}) = &\int_{f_4}\left[-Q_t^n(\mathbf{Y})\frac{e^{-i\kappa R}(i\kappa R+1)}{4\pi R^2}\frac{(r'-r\cos(\theta-\theta'))}{R}\right]dS\\ &+\int_{f_5}\left[-Q_t^n(\mathbf{Y})\frac{e^{-i\kappa R}(i\kappa R+1)}{4\pi R^2}\frac{(Z'-Z)}{R}-\frac{\partial Q_t^n(\mathbf{Y})}{\partial Z}\frac{e^{-i\kappa R}}{4\pi R}\right]dS\\ &+\int_{f_6}\left[Q_t^n(\mathbf{Y})\frac{e^{-i\kappa R}(i\kappa R+1)}{4\pi R^2}\frac{(Z'-Z)}{R}+\frac{\partial Q_t^n(\mathbf{Y})}{\partial Z}\frac{e^{-i\kappa R}}{4\pi R}\right]dS.\end{aligned} \tag{23}$$

All of the above expressions are suitable for arbitrarily distributed, circumferentially or axially segmented, locally reacting liners.

2.2. Numerical implementation

The boundary integral Eq. (18) is numerically discretized as follows:

$$A_{p1}(\mathbf{y}_i,\mathbf{y}_j)Q_1^n(y_j)+A_{p2}(\mathbf{y}_i,\mathbf{y}_j)Q_2^n(\mathbf{y}_j)+A_{p3}(\mathbf{y}_i,\mathbf{y}_j)Q_3^n(\mathbf{y}_j)+A_{v2}(\mathbf{y}_i,\mathbf{y}_j)Q_{Z2}^n(\mathbf{y}_j)+A_{v3}(\mathbf{y}_i,\mathbf{y}_j)Q_{Z3}^n(\mathbf{y}_j)=Q_i^n(\mathbf{y}_i), \tag{24}$$

where $Q_1^n(\mathbf{y}_j)$ is the $Q_t{}^n$ of the point $\mathbf{y}_j$ on the f_1 surface, $Q_2^n(\mathbf{y}_j)$ is the $Q_t{}^n$ of the point $\mathbf{y}_j$ on the f_2 surface, $Q_3^n(\mathbf{y}_j)$ is the $Q_t{}^n$ of the point $\mathbf{y}_j$ on the f_3 surface, $Q_{Z2}^n(\mathbf{y}_j)$ is the $\partial Q_t{}^n/\partial Z$ of the point $\mathbf{y}_j$ on the f_2 surface, $Q_{Z3}^n(\mathbf{y}_j)$ is the $\partial Q_t{}^n/\partial Z$ of the point $\mathbf{y}_j$ on the f_3 surface and $Q_i^n(\mathbf{y}_i)$ is the $Q_i{}^n$ of the point $\mathbf{y}_i$ on all the interior surfaces of the duct. The coefficients are expressed as

$$A_{p1i,j}=\frac{1}{2}\delta_{ij}-\frac{e^{-i\kappa R_{ij}}(i\kappa R_{ij}+1)}{4\pi R_{ij}^2}\frac{(r_j'-r_i\cos(\theta_i-\theta_j'))}{R_{ij}}\Delta S_{1j}, \tag{25}$$

$$A_{p2i,j}=-\frac{e^{-i\kappa R_{ij}}(i\kappa R_{ij}+1)}{4\pi R_{ij}^2}\frac{(Z_j'-Z_i)}{R_{ij}}\Delta S_{2j}, \tag{26}$$

$$A_{p3i,j}=\frac{e^{-i\kappa R_{ij}}(i\kappa R_{ij}+1)}{4\pi R_{ij}^2}\frac{(Z_j'-Z_i)}{R_{ij}}\Delta S_{3j}, \tag{27}$$

$$A_{v2i,j}=-\frac{e^{-i\kappa R_{ij}}}{4\pi R_{ij}}\Delta S_{2j}, \tag{28}$$

$$A_{v3i,j}=\frac{e^{-i\kappa R_{ij}}}{4\pi R_{ij}}\Delta S_{3j}, \tag{29}$$

where ΔS_j is the area of the surface grid element.

The boundary integral Eq. (19) is numerically discretized as follows:

$$A_{p4}(\mathbf{y}_i,\mathbf{y}_j)Q_4^n(\mathbf{y}_j)+A_{p5}(\mathbf{y}_i,\mathbf{y}_j)Q_5^n(\mathbf{y}_j)+A_{p6}(\mathbf{y}_i,\mathbf{y}_j)Q_6^n(\mathbf{y}_j)+A_{v5}(y_i,y_j)Q_{Z5}^n(\mathbf{y}_j)+A_{v6}(\mathbf{y}_i,\mathbf{y}_j)Q_{Z6}^n(\mathbf{y}_j)=0, \tag{30}$$

where $Q_4^n(\mathbf{y}_j)$ is the $Q_t{}^n$ of the point $\mathbf{y}_j$ on the f_4 surface, $Q_5^n(\mathbf{y}_j)$ is the $Q_t{}^n$ of the point $\mathbf{y}_j$ on the f_5 surface, $Q_6^n(\mathbf{y}_j)$ is the $Q_t{}^n$ of the point $\mathbf{y}_j$ on the f_6 surface, $Q_{Z5}^n(\mathbf{y}_j)$ is the $\partial Q_t{}^n/\partial Z$ of the point $\mathbf{y}_j$ on the f_5 surface and $Q_{Z6}^n(\mathbf{y}_j)$ is the $\partial Q_t{}^n/\partial Z$ of the point $\mathbf{y}_j$ on the f_6 surface. The coefficients are expressed as

$$A_{p4i,j}=\frac{1}{2}\delta_{ij}+\frac{e^{-i\kappa R_{ij}}(i\kappa R_{ij}+1)}{4\pi R_{ij}^2}\frac{(r_j'-r_i\cos(\theta_i-\theta_j'))}{R_{ij}}\Delta S_{4j}, \tag{31}$$

$$A_{p5i,j}=\frac{e^{-i\kappa R_{ij}}(i\kappa R_{ij}+1)}{4\pi R_{ij}^2}\frac{(Z_j'-Z_i)}{R_{ij}}\Delta S_{5j}, \tag{32}$$

$$A_{p6i,j}=-\frac{e^{-i\kappa R_{ij}}(i\kappa R_{ij}+1)}{4\pi R_{ij}^2}\frac{(Z_j'-Z_i)}{R_{ij}}\Delta S_{6j}, \tag{33}$$

$$A_{v5i,j}=\frac{e^{-i\kappa R_{ij}}}{4\pi R_{ij}}\Delta S_{5j}, \tag{34}$$

$$A_{v6i,j}=-\frac{e^{-i\kappa R_{ij}}}{4\pi R_{ij}}\Delta S_{6j}. \tag{35}$$

Notice that Eq. (18) is suitable for the hard interior duct. Eq. (17) has one more term

$$\int_{f_1}\left[\frac{\mathrm{i}Ma^2\mathrm{e}^{-\mathrm{i}\kappa R}}{4\pi R\beta^3 zn\kappa}\left(\frac{\partial^2 Q_t^n(\mathbf{Y})}{\partial Z^2}-\frac{2\mathrm{i}\kappa}{Ma}\frac{\partial Q_t^n(\mathbf{Y})}{\partial Z}-\frac{\kappa^2}{Ma^2}Q_t^n(\mathbf{Y})\right)\right]\mathrm{d}S$$

than Eq. (18) when the liners are laid on the interior wall of the duct. The integral surface of this term only covers where the liners are actually laid on. The partial differential terms $\partial^2 Q_t{}^n/\partial Z^2$ and $\partial Q_t{}^n/\partial Z$ can be expressed with the differential schemes about $Q_t{}^n$. Then another term $B_{p1}(\mathbf{y}_i,\mathbf{y}_j)Q_1^n(\mathbf{y}_j)$ should be added on the left-hand side of Eq. (24) when the point y_j is located on the interior wall with liners. The coefficient $B_{p1}(\mathbf{y}_i,\mathbf{y}_j)$ will be different with different differential schemes about $Q_t{}^n$ and the expression will not be presented here. In nature the acoustic pressure differs hardly whichever the schemes adopted.

The number of unknown variables in Eqs. (24) and (30) are both five and the number of the integral surfaces are three. In order to obtain a closed equation group, it is necessary to add the continuous conditions on the duct openings, which are

$$Q_2^n(\mathbf{y}_j)=Q_5^n(\mathbf{y}_j)\quad Q_3^n(\mathbf{y}_j)=Q_6^n(\mathbf{y}_j), \tag{36a,b}$$

$$Q_{Z2}^n(\mathbf{y}_j)=Q_{Z5}^n(\mathbf{y}_j)\quad Q_{Z3}^n(\mathbf{y}_j)=Q_{Z6}^n(\mathbf{y}_j). \tag{37a,b}$$

The matrix equation group is as follows:

$$\begin{pmatrix} A_{p1} & A_{p2} & A_{p3} & 0 & A_{v2} & A_{v3}\\ A_{p1} & A_{p2} & A_{p3} & 0 & A_{v2} & A_{v3}\\ A_{p1} & A_{p2} & A_{p3} & 0 & A_{v2} & A_{v3}\\ 0 & A_{p5} & A_{p6} & A_{p4} & A_{v5} & A_{v6}\\ 0 & A_{p5} & A_{p6} & A_{p4} & A_{v5} & A_{v6}\\ 0 & A_{p5} & A_{p6} & A_{p4} & A_{v5} & A_{v6} \end{pmatrix}\begin{pmatrix} Q_1^n\\ Q_2^n\\ Q_3^n\\ Q_4^n\\ Q_{Z2}^n\\ Q_{Z3}^n \end{pmatrix}=\begin{pmatrix} Q_{1i}^n\\ Q_{2i}^n\\ Q_{3i}^n\\ 0\\ 0\\ 0 \end{pmatrix}, \tag{38}$$

where $Q_{1i}{}^n$, $Q_{2i}{}^n$ and $Q_{3i}{}^n$ represent the Q_i^n of the incident acoustic pressure on the f_1, f_2 and f_3 surfaces, respectively. The $Q_t{}^n$ and $\partial Q_t{}^n/\partial Z$ on every discrete point x_j can be obtained by solving Eq. (38). Then the acoustic pressure of any point inside or outside the duct can be obtained through Eqs. (22), (23) and (10).

2.3. Verification and investigation

The directivity predictions of the axisymmetric cases are used to validate the 3D BIEM program. The cases with the same acoustic parameters, duct geometry and spinning axial dipoles sources in Ref. [11] are used for comparisons. Both the radius a and the length L of the duct are 1 m. The incident acoustic sources are $B=20$ spinning axial dipoles, which lie at the same radius $r'_0=0.9a$ with a uniform interval in circumference, located on the duct middle plane $Z=0$. The thrust F_T of each point source is 50 N. The flight Mach number is 0.4 and the Helmholtz number ka is 24.4. The liner configurations are outlined in Table 1.

Figs. 3–5 show the comparisons of directivity predicted by the 3D approach and the 2D approach for the same cases as that shown in Figs. 4–6 of Ref. [11], respectively, but herewith the origin of sound pressure level (SPL) is from 0 dB for comparing with the following non-uniform liner cases, and in Ref. [11] it is from 90 dB

Table 1
Liner axis location and parameters for 3D finite duct model verification

Liner configuration	Liner axis location (m)	Specific impedance
1	−0.5–0.5	Hard
2	0.0–0.4	$0.5+0.5i$
3	−0.4–0.0; 0.0–0.4	2; $0.5+0.5i$

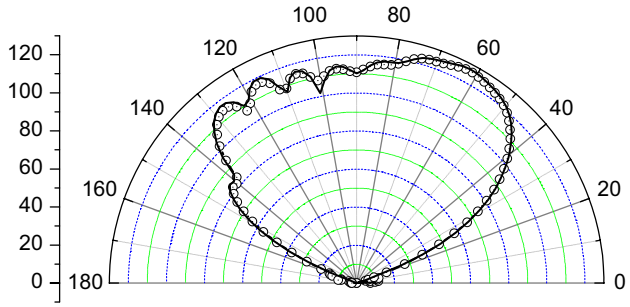

Fig. 3. Directivity comparison between 3D and axisymmetric predictions; configuration 1; —⊙—, 3D prediction; —, axisymmetric prediction.

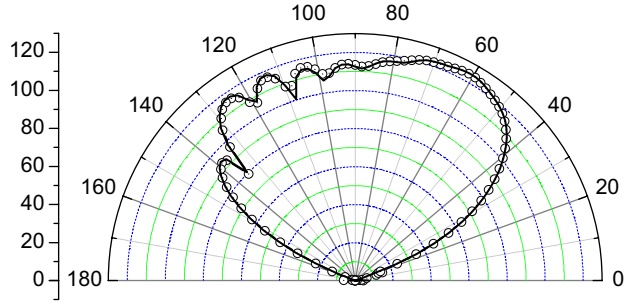

Fig. 4. Directivity comparison between 3D and axisymmetric predictions; configuration 2; —⊙—, 3D prediction; —, axisymmetric prediction.

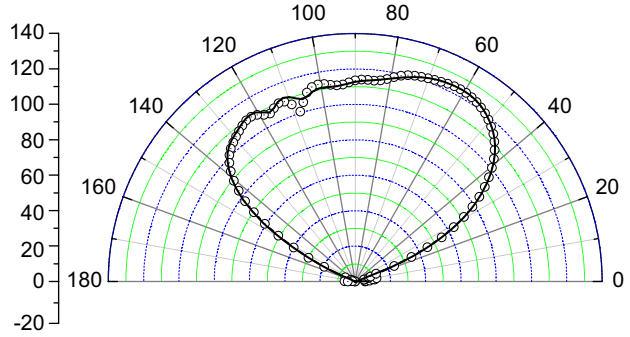

Fig. 5. Directivity comparison between 3D and axisymmetric predictions; configuration 3; —⊙—, 3D prediction; —, axisymmetric prediction.

Table 2
Liner configurations for investigating the hard-splices' influence on finite duct

Liner configuration	Splice number	Splice location	Splice configuration
4	1	0–5°	Periodic
5	2	0–5°; 180–185°	Periodic
6	4	0–5°; 90–95°; 180–185°; 270–275°	Periodic
7	4	0–5°; 70–75°; 200–205°; 270–275°	Non-periodic

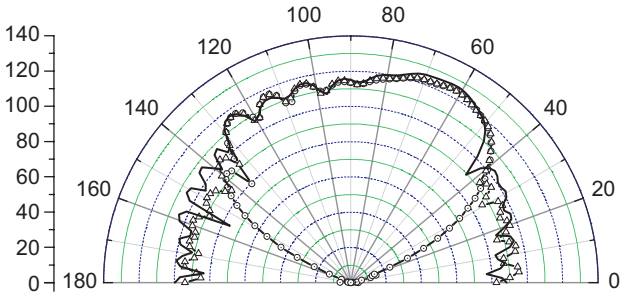

Fig. 6. Directivity comparisons of different hard-splice numbers; configurations 2, 4 and 5; —⊙—, configuration 2; –△–, configuration 4; —, configuration 5.

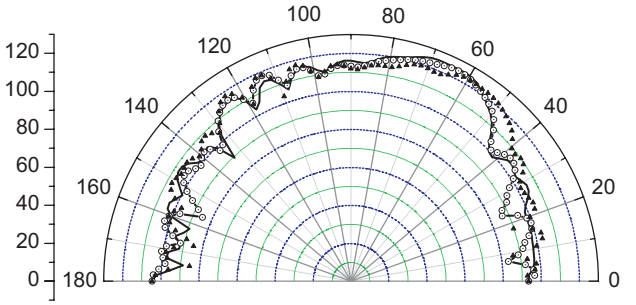

Fig. 7. Directivity comparisons on $\theta = 0$, $\theta = 120$, $\theta = 240$ planes; configuration 7; —, $\theta = 0$; —⊙—, $\theta = 120$, ▲, $\theta = 240$.

for the purpose of comparing with the results of TBIEM-3D [12]. The figures show a relatively good agreement between the 3D and the axisymmetric predictions.

To investigate the influence of hard-splices of liners on the duct acoustic radiation and propagation, a series of liner configurations with different splice numbers and locations are selected, as listed in Table 2. The axial locations of all the liners are at 0–0.4, as that of configuration 2 listed in Table 1. The directivity comparisons of liner configurations 2, 4 and 5 are displayed in Fig. 6; the observer points are located at a semicircle on $\theta = 0$ plane in a cylindrical frame (r, θ, Z). The radius of the semicircle is 10 m and the center is the duct center point. Although the directivities on different θ planes will be different when the hard-splices exist, only the directivities on $\theta = 0$ plane are presented in Fig. 6 for offering a qualitative comparison between the circumferentially non-uniform and the uniform boundary. The directivity comparisons of different θ planes will be presented in Fig. 7 which illustrate that the directivity on the $\theta = 0$ plane is enough for qualitative analyses.

In Fig. 6 it is obvious that the acoustic pressure near the axis is up to about 100 dB when the hard-splices exist, and it is close to zero when no hard-splices exist. The circumferentially non-uniform boundary condition can cause an acoustic pressure accumulation near the duct axis, while it may be counteracted by a circumferentially uniform boundary. In Fig. 6 the angles of the greatest SPL corresponding to different configurations are approximately the same and the greatest SPL of the non-uniform liners are a slightly greater than that of a uniform liner.

Liner configuration 7 in Table 2 is chosen as a representative case to illustrate the influence of more general hard-splice distribution, circumferentially non-periodic. Fig. 7 gives the directivity comparisons of configuration 7 on three θ planes: $\theta = 0$, 120 and 240. Although the values have a little differ slightly on different θ planes, the angles and values of the greatest SPL are approximately the same and the values near the axis are also up to 100 dB. This indicates that the directivity on the $\theta = 0$ plane could reasonably provide a qualitative analyses.

The instantaneous pressure contours on a circular cross-section in the middle of the liner are presented in Figs. 8–11 (configurations 2, 5–7) for a qualitative understanding of the influence of hard-splices on the

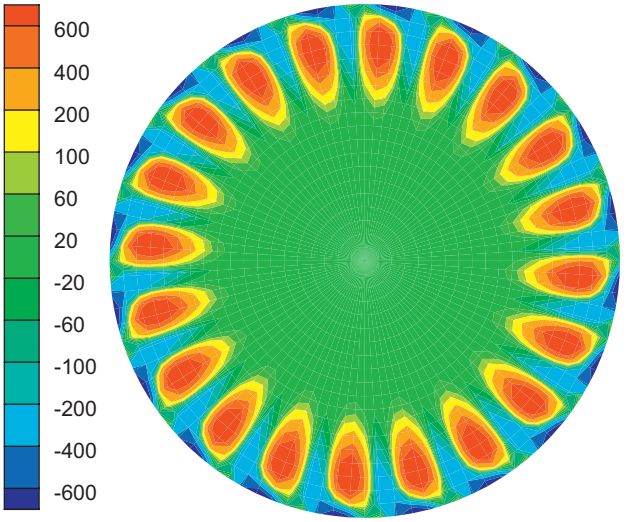

Fig. 8. Instantaneous acoustic pressure contour on a specific cross-section; configuration 2.

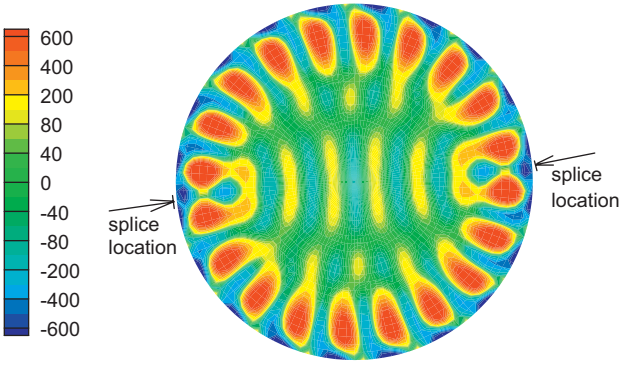

Fig. 9. Instantaneous acoustic pressure contour on a specific cross-section; configuration 5.

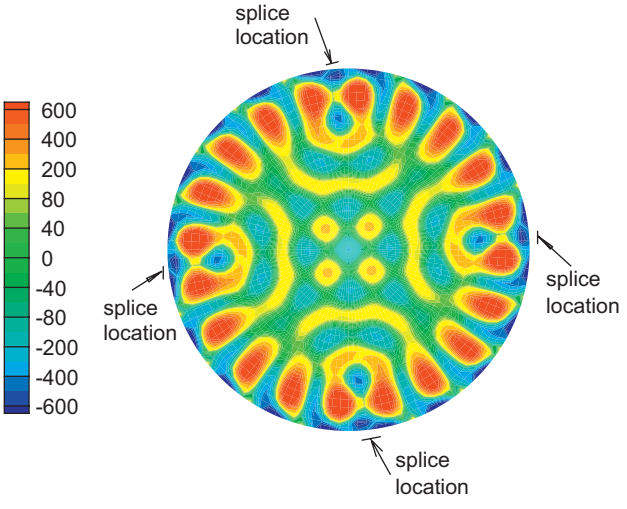

Fig. 10. Instantaneous acoustic pressure contour on a specific cross-section; configuration 6.

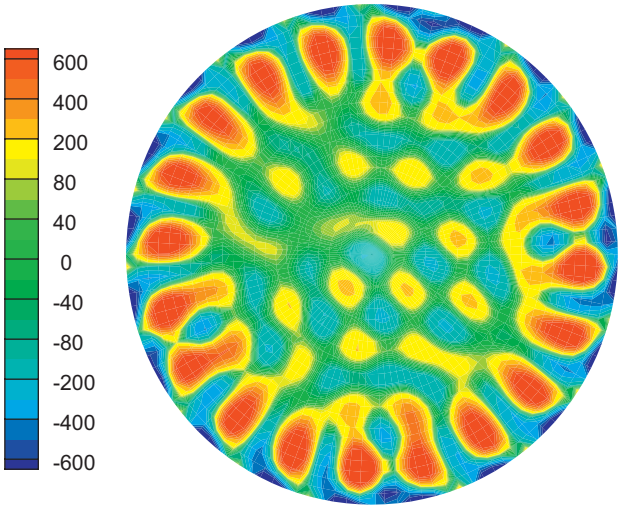

Fig. 11. Instantaneous acoustic pressure contour on a specific cross-section; configuration 7.

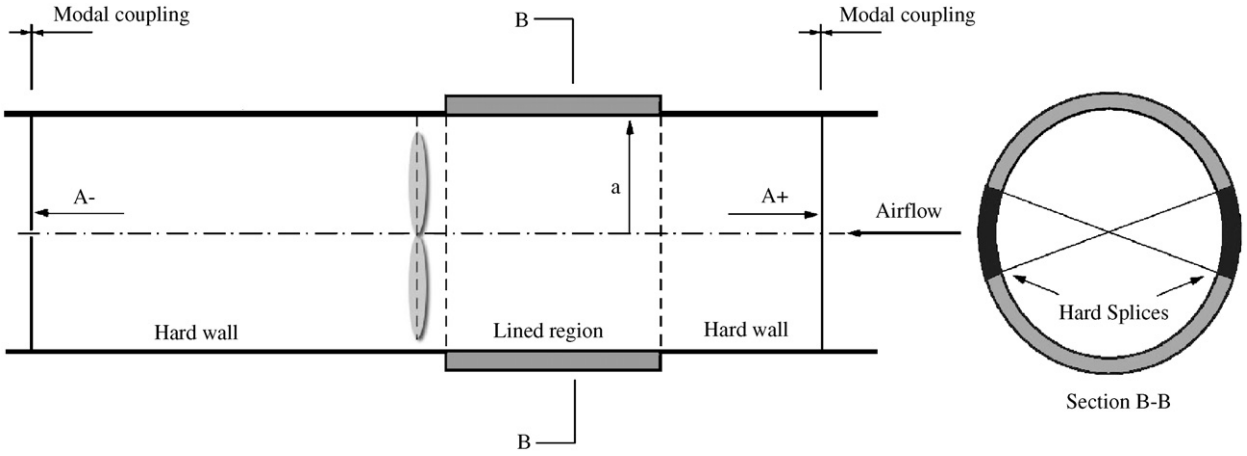

Fig. 12. Sketch map of an infinite length duct model.

acoustic propagation. The hard-splices in Figs. 8–10 are circumferentially periodic, while the hard-splices in Figs. 11 are circumferentially non-periodic. The hard-splice locations can be easily recognized in Figs. 8–10. This phenomenon can be explained by the mode scattering mechanism, which will be discussed in the following infinite duct model investigation.

3. Infinite duct model by BIEM

3.1. Physical model and numerical implementation

As can be seen from the sketch of the infinite duct model illustrated in Fig. 12, the same acoustic sources as that of the finite duct model are situated on a specific cross-section. The region between the upstream and downstream planes is manipulated in the same way as that in the finite duct model. Hence BIEM and Eqs. (17) and (22) could be used to calculate the acoustic field in the region. The acoustic field outside the region is expressed by a combination of acoustic modes in an infinite circular duct which implies the non-reflecting boundary. The continuous conditions on the surfaces are used to couple the inside and outside acoustic field.

The acoustic pressure outside the region is expressed by the following series:

$$p = \sum_{m_0=-M}^{M} \sum_{n_0=1}^{N} A^{\pm}_{m_0 n_0} J_{m_0}(k_{r,m_0 n_0} r) \mathrm{e}^{-\mathrm{i}m_0\theta + \mathrm{i}k_Z^{\pm} Z'}, \tag{39}$$

where Z' is the axis coordinate in the axially moving frame and m_0 is the circumferential mode order, which may be positive or negative. It is necessary to include both the positive and the negative modes in the analyses since the asymmetry of the liner will excite modes in both circumferential directions. The circumferential and the radial modes should cover all the cut-on modes and a few cut-off modes. The radial order n_0 is specified from 1; the mode of (0,1) represents the plane wave. $k_{r,m_0 n_0}$ is the n_0th radial wavenumber for the m_0th circumferential mode and is the n_0th solution of the eigenvalue problem

$$J'_{m_0}(k_{r,m_0 n_0} a) = 0. \tag{40}$$

The axial wavenumber ${k_Z}^{\pm}$ is

$$k_Z^{\pm} = \begin{cases} \dfrac{-Mak \mp \sqrt{k^2 - (1-Ma^2)k_{r,m_0 n_0}}}{1-Ma^2} & \text{cut-on,} \\ \dfrac{-Mak \pm \mathrm{i}\sqrt{(1-Ma^2)k_{r,m_0 n_0} - k^2}}{1-Ma^2} & \text{cut-off.} \end{cases} \tag{41}$$

The boundary integral equations (17) and (22) are expressed in the axially moving stretched frame and Eqs. (39)–(41) are expressed in the axially moving frame, so that $Z' = \beta Z$.

On the upstream/downstream planes, the coupling conditions are expressed as

$$Q_t^n(r,\theta,Z)\,\mathrm{e}^{-\mathrm{i}\kappa MaZ} = \sum_{m_0=-M}^{M} \sum_{n_0=1}^{N} A^{\pm}_{m_0 n_0} J_{\mathrm{m}_0}(k_{r,m_0 n_0} r)\,\mathrm{e}^{-\mathrm{i}m_0\theta + \mathrm{i}k_Z^{\pm} Z\beta}, \tag{42}$$

$$\frac{\partial Q_t^n}{\partial Z} = \sum_{m_0=-M}^{M} \sum_{n_0=1}^{N} (\mathrm{i}\kappa Ma + \mathrm{i}k_Z^{\pm}\beta) A^{\pm}_{m_0 n_0} J_{m_0}(k_{r,m_0 n_0} r)\,\mathrm{e}^{-\mathrm{i}m_0\theta + \mathrm{i}k_Z^{\pm} Z\beta}\,\mathrm{e}^{\mathrm{i}\kappa MaZ}. \tag{43}$$

The conjugate orthogonal condition of modes is used to determine the modal coefficients $A^{+}_{m_0 n_0}$ and $A^{-}_{m_0 n_0}$. The eigenfunction is expressed as

$$E_{m_0 n_0}(r,\theta) = J_{m_0}(k_{r,m_0 n_0} r)\,\mathrm{e}^{-\mathrm{i}m_0\theta}, \tag{44}$$

then the conjugate of $E_{m_0 n_0}$ is

$$E^*_{m_0 n_0}(r,\theta) = J_{m_0}(k_{r,m_0 n_0} r)\,\mathrm{e}^{\mathrm{i}m_0\theta}. \tag{45}$$

If $m_0 \neq m'_0$ or $n_0 \neq n'_0$,

$$\int_0^{2\pi} \int_0^{a} E_{m_0 n_0}(r,\theta) E^*_{m'_0 n'_0}(r,\theta) r\,\mathrm{d}r\,\mathrm{d}\theta = 0. \tag{46}$$

If $m_0 = m'_0$ and $n_0 = n'_0$,

$$\int_0^{2\pi} \int_0^{a} E_{m_0 n_0}(r,\theta) E^*_{m_0 n_0}(r,\theta) r\,\mathrm{d}r\,\mathrm{d}\theta = \pi\left(a^2 - \frac{m_0^2}{k^2_{r,m_0 n_0}}\right) J^2_{m_0}(k_{r,m_0 n_0} a). \tag{47}$$

Combining Eqs. (46) and (47) with (42), the matrix equation is obtained on the upstream/downstream modal coupling planes

$$\begin{pmatrix} a_{11} & \cdots & a_{1K} \\ \vdots & \ddots & \vdots \\ a_{K1} & \cdots & a_{KK} \end{pmatrix} \begin{pmatrix} Q^n_{t1} \\ \vdots \\ Q^n_{tK} \end{pmatrix} + \begin{pmatrix} b_{11} & & \mathbf{0} \\ & \ddots & \\ \mathbf{0} & & b_{KK} \end{pmatrix} \begin{pmatrix} A^{\pm}_{-M0} \\ \vdots \\ A^{\pm}_{MN} \end{pmatrix} = \begin{pmatrix} 0 \\ 0 \\ 0 \end{pmatrix}, \tag{48}$$

where $K=(2M+1)*N$ is the total mode number including all the combinations of circumferential modes and radial modes. The elements in the coefficient matrixes are

$$a_{ij}=\int_{\theta_i}^{\theta_i+\Delta\theta}\int_{r_j}^{r_j+\Delta r}J_{m_0}(k_{r,m_0n_0}r)\,\mathrm{e}^{\mathrm{i}m_0\theta}r\,\mathrm{d}r\,\mathrm{d}\theta, \tag{49}$$

$$b_{ii}=-\pi\left(a^2-\frac{m_0^2}{k_{r,m_0n_0}^2}\right)J_{m_0}^2(k_{r,m_0n_0}a)\,\mathrm{e}^{\mathrm{i}k_Z^{\pm}Z\beta}\mathrm{e}^{\mathrm{i}\kappa MaZ}. \tag{50}$$

Combining Eqs. (46) and (47) with (43), another matrix equation is obtained

$$\begin{pmatrix}a_{11}&\cdots&a_{1K}\\ \vdots&\ddots&\vdots\\ a_{K1}&\cdots&a_{KK}\end{pmatrix}\begin{pmatrix}\frac{\partial Q_{t1}^n}{\partial Z}\\ \vdots\\ \frac{\partial Q_{tK}^n}{\partial Z}\end{pmatrix}+\begin{pmatrix}b'_{11}&&\mathbf{0}\\ &\ddots&\\ \mathbf{0}&&b'_{KK}\end{pmatrix}\begin{pmatrix}A_{-M0}^{\pm}\\ \vdots\\ A_{MN}^{\pm}\end{pmatrix}=\begin{pmatrix}0\\0\\0\end{pmatrix}, \tag{51}$$

where a_{ij} is the same as that in Eq. (48) and b'_{ij} is

$$b'_{ii}=-\pi\left(a^2-\frac{m_0^2}{k_{r,m_0n_0}^2}\right)J_{m_0}^2(k_{r,m_0n_0}a)(\mathrm{i}\kappa Ma+\mathrm{i}k_Z^{\pm}\beta)\mathrm{e}^{\mathrm{i}k_Z^{\pm}Z\beta}\mathrm{e}^{\mathrm{i}\kappa MaZ}. \tag{52}$$

The discrete grid point number on the upstream/downstream modal coupling planes is equal to K; then, the Q_t^n and $\partial Q_t^n/\partial Z$ at every discrete point x_j on the interior surfaces of the duct and the modal coefficients $A_{m_0n_0}^{\pm}$ can be obtained by solving Eqs. (24), (48) and (51) together.

3.2. Verification and investigation

The verification is performed by comparing the prediction with a known analytical solution of an infinite duct with a hard wall [13]. For the spinning point sources at r'_0, the analytical solution in a moving stretched frame is

$$p'(r,\theta,Z)=-\frac{BF_T}{2}\sum_{m_0=-\infty}^{\infty}\sum_{n_0=1}^{\infty}\frac{J_{m_0}(k_{r,m_0n_0}r)J_{m_0}(k_{r,m_0n_0}r'_0)k_Z^{\pm}\mathrm{e}^{\mathrm{i}k_Z^{\pm}Z\beta-\mathrm{i}m_0\theta}}{\pi(a^2-(m_0^2/k_{r,m_0n_0}^2))J_{m_0}^2(k_{r,m_0n_0}a)\kappa_{n_0m_0}}, \tag{53}$$

where

$$\kappa_{n_0m_0}=\begin{cases}\sqrt{k^2-(1-Ma^2)k_{r,m_0n_0}^2} & \text{cut-on},\\ -\mathrm{i}\sqrt{(1-Ma^2)k_{r,m_0n_0}^2-k^2} & \text{cut-off}.\end{cases} \tag{54}$$

Fig. 13 shows an instantaneous pressure distribution on the axis section inside the duct; the left half of the contour is from the analytical solution (53), and the right half is from the numerical calculation. The duct radius is 0.2 m with an axial inflow Mach number 0.4, containing two spinning point sources at the radius $r'_0=0.9a$ with $F_T=50$ N, which means the incident fundamental circumferential mode is second order, and $ka=4.4$. The comparison in Fig. 13 shows a good agreement and the difference of $A_{m_0n_0}^{\pm}$ obtained by BIEM and the analytical solution is in the range of 12%, which is listed in Table 3. The infinite duct model is verified by these comparisons.

Then five liner configurations outlined in Table 4 are selected to investigate the mode scattering phenomena excited by a circumferentially non-uniform boundary condition. The acoustic parameters and duct geometry are the same as those used in the above infinite duct case. When ka is 4.4, the modes (0,1) (0,2) ($\pm$1,1) ($\pm$2,1) and ($\pm$3,1) are cut-on. The liner with a length of 0.2 m is located 0.1 m away from the source plane in the upstream. The hard-splices in configurations 8–11 are periodically distributed in the circumferential direction. It is anticipated by the rotor–stator interaction mechanism that the circumferential mode orders excited by the

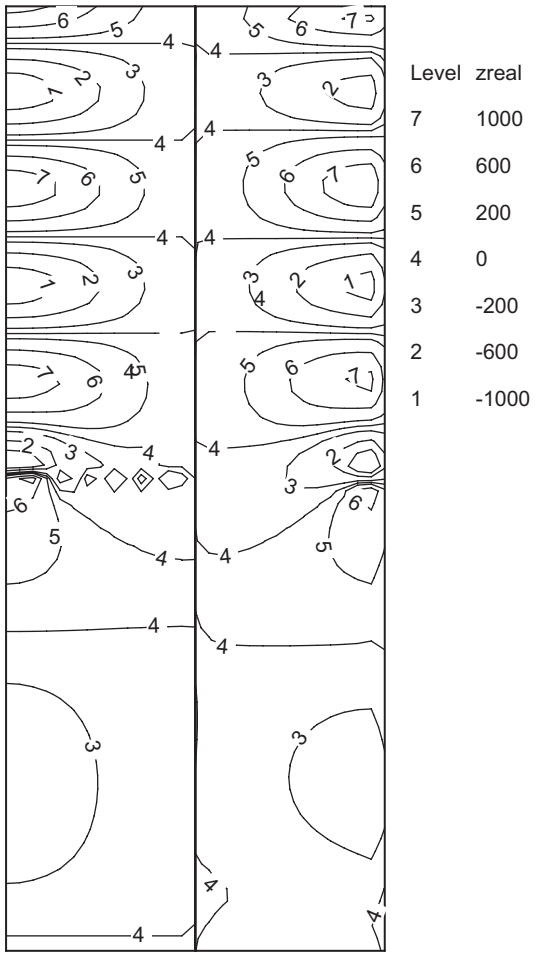

Fig. 13. Instantaneous acoustic pressure isoline comparison between analysis solution and the infinite length duct model; the left half presents an analytical solution; the right half presents a numerical calculation.

Table 3
Amplitude value of $A^{+}_{m_0 n_0}$ and $A^{-}_{m_0 n_0}$ by BIEM and analytical solution

Modal coefficient	Analytical solution	BIEM	Difference (%)
$A^{+}_{m_0 n_0}$	2521.1	2270	9.96
$A^{-}_{m_0 n_0}$	799.6	705	11.83

Table 4
Liner configurations for investigating mode scattering in an infinite duct model

Liner configuration	Splice number	Splice location	Splice configuration
8	0	None	–
9	1	0–10°	Periodic
10	2	0–10°; 180–190°	Periodic
11	3	0–10°; 120–130°; 240–250°	Periodic
12	3	0–10°; 100–110°; 200–210°	Non-periodic

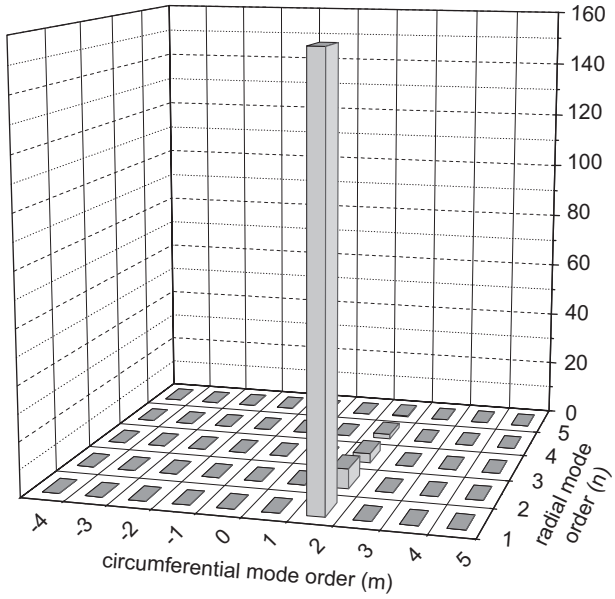

Fig. 14. Modal spectrum of a cut-on incident mode; configuration 8.

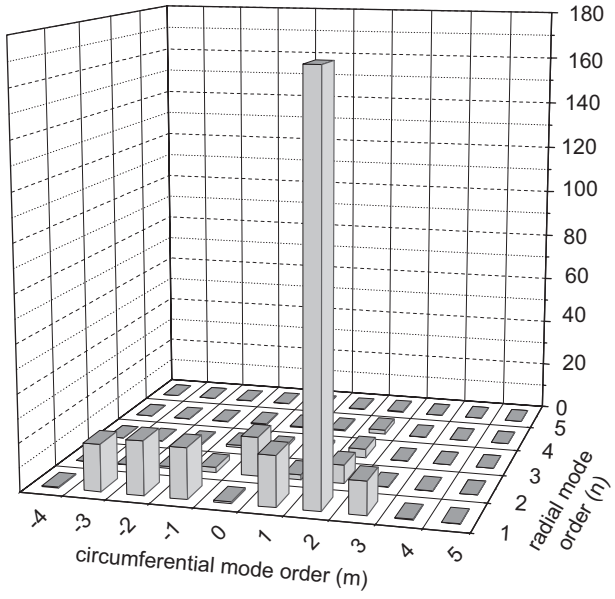

Fig. 15. Modal spectrum of a cut-on incident mode; configuration 9.

scattering from periodic splices will be specified by the sequence

$$m_0 = m_I \pm lJ, \tag{55}$$

where m_I is the circumferential mode order of the incident wave, l is an arbitrary integer and J is the number of splices distributed periodically in circumference.

The modal spectra of the amplitude of $A^{+}_{m_0 n_0}$ at the cross-section 0.6 m apart from the source plane in the upstream are presented in Figs. 14–17 where the modes determined by Eq. (55) can be visualized clearly. The number of hard-splices is zero in liner configuration 8, and so only the incident circumferential mode (second order) exists in Fig. 14. It is noticed that a few cut-off radial modes appear in all the following modal spectra

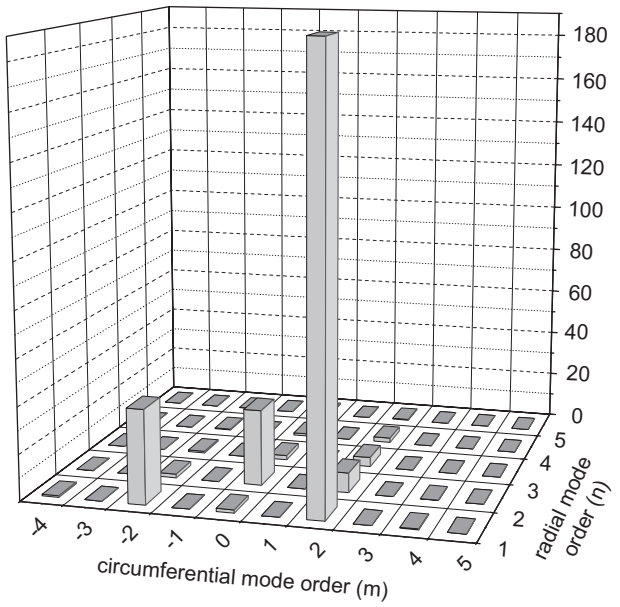

Fig. 16. Modal spectrum of a cut-on incident mode; configuration 10.

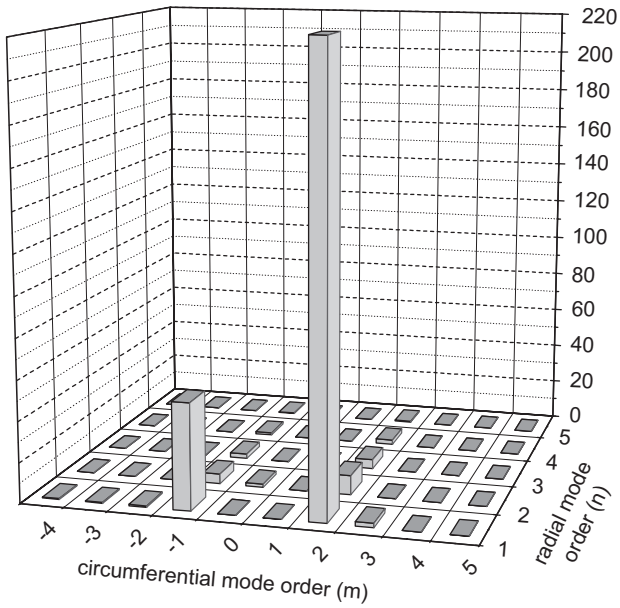

Fig. 17. Modal spectrum of a cut-on incident mode; configuration 11.

especially at the incident circumferential mode. This is because the incident source used in our model is in free space. All the radial modes are included in our incident source and so they inevitably appear in the modal spectra although they are cut-off and attenuate quickly. It can be seen that their values are very small compared with the prevailing modes. In fact, this kind of incident source including all the radial modes is closer to the actual situation than only one single mode as the input source.

The number of hard-splices is one in liner configuration 9; according to Eq. (55) and the cut-on condition, all the cut-on circumferential mode orders $\pm$1st, 0th, $\pm$2nd and $\pm$3rd are excited and all the cut-on modes (0,2)

($\pm$1,1) ($\pm$2,1) and ($\pm$3,1) are evident in Fig. 15 except for the plane wave (0,1), which is absent when the incident sources are non-uniform in the radial direction. The number of hard-splices is two in liner configuration 10; the circumferential mode orders—2nd and 0th are excited and distinct as modes (−2,1) and (0,2) in Fig. 16. Only the modes (−1,1) and (2,1) given in Fig. 17 for liner configuration 11 have three hard-splices.

It is assumed that every cut-on circumferential mode will be excited by circumferentially non-periodic hard-splices. Configuration 12 is one case with a non-periodic hard-splices liner. All the cut-on circumferential mode orders $\pm$1st, 0th, $\pm$2nd and $\pm$3rd are excited. In Fig. 18 all the cut-on modes except for the plane wave are observed. The modal spectrum of the circumferentially non-periodic hard-splices liner case is similar to that with only one hard-splice, and so the circumferential modes excited in Fig. 18 are the same as those in Fig. 15.

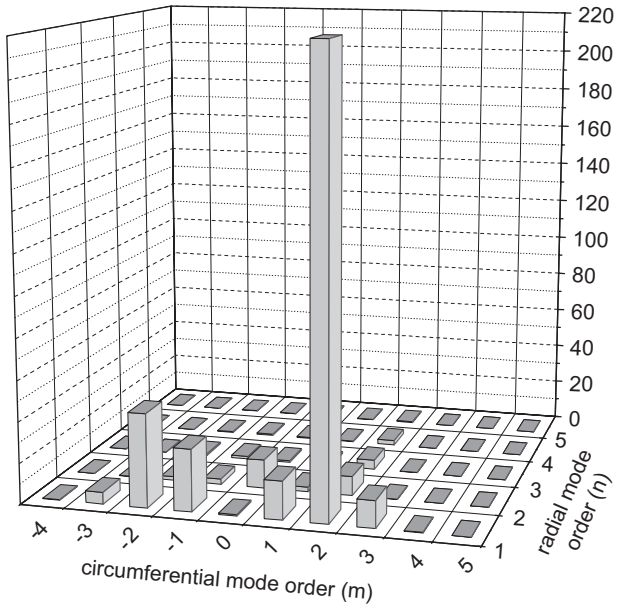

Fig. 18. Modal spectrum of a cut-on incident mode; configuration 12.

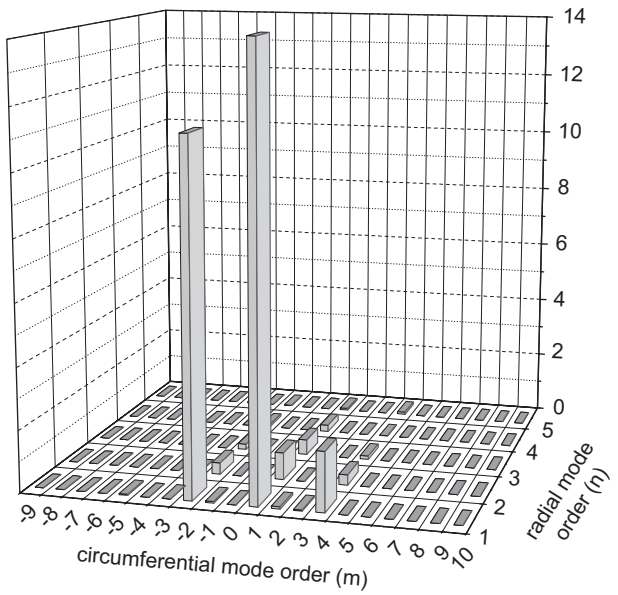

Fig. 19. Modal spectrum of a cut-off incident mode; configuration 11.

Then liner configuration 11 is taken to consider the situation of cut-off incident mode1, where the incident circumferential mode is increased to 4, which is beyond the cut-on modes for $ka = 4.4$ and the other parameters are maintained the same as the above illustrations. The number of hard-splices of configuration 11 is three, and according to Eq. (55) the -2nd and 1st circumferential modes will be excited, and be cut-on based on the ducted acoustics; these modes still appear in Fig. 19, although the amplitudes of the scattered cut-on modes are greater than that of the cut-off incident mode, but they are too small to be included in the acoustic liners' design process.

The mechanism of mode scattering caused by hard-splices liners is revealed by the infinite duct model. The fact that the locations of hard-splices are visualized can be explained by the mode scattering mechanism.

4. Conclusions

A 3D BIEM is developed and verified, which deals with the ducted-fan noise of a finite cylindrical duct with an axially uniform inflow. The acoustic liners inside a duct are allowed to be circumferentially or axially non-uniform. The influence of the longitudinal hard-splices of liners, due to manufacturing, on the duct acoustic radiation and propagation is discussed. Four liner configurations with different hard-splice locations and numbers are investigated. It is observed from the radiation directivities that the acoustic pressure near the axis is increased and is up to about 100 dB when the hard-splices exist, but it is near zero in the uniform liner case. The angles of the greatest SPL for different configurations are approximately the same and the greatest SPL of the non-uniform liners is a slightly greater than that of a uniform liner. In the contours of liners' across section, the locations of hard-splices could be easily recognized for the cases of circumferentially periodically distributed hard-splices.

In order to investigate the mode scattering phenomena caused by hard-splices, a 3D infinite duct model is developed. The BIEM is used for the acoustic field between the upstream/downstream planes, where coupling conditions are implemented to match the boundary integration with the analytical series. Then the modal coefficients of the upstream and downstream have been obtained, and the mode scattering phenomena have been observed. Through the spectra of modal coefficients it is found that for the circumferentially periodically distributed hard-splices the modal scattering mechanism is similar to that of the rotor-stator interaction, and for the circumferentially non-periodically distributed hard-splices almost all of the cut-on circumferential modes could be excited. Although the hard-splices could scatter out cut-on modes from the cut-off incident mode, the effects of excited cut-on modes are too minor to be included in the ducted-fan noise prediction.

It is concluded that the present finite duct model does provide an accurate and rapid noise prediction tool for engineering purposes with an emphasis on the effect of hard-splices on duct acoustic propagation and radiation. Furthermore, it could be a good verification tool for other numerical simulations.

References

[1] S.L. Sarin, E.R. Rademaker, In-flight acoustic mode measurements in the turbofan engine inlet of Fokker 100 aircraft, AIAA-93-4414.
[2] E.R. Rademaker, S.L. Sarin, C.A. Parente, Experimental investigation on the influence of liner non-uniformities on prevailing modes (of acoustic propagation in turbofan engines), AIAA-96-30799.
[3] B.A. Regan, J.A. Eaton, Finite element investigation of the influence of liner splices on duct modes, AIAA-98-2313.
[4] B.A. Regan, J.A. Eaton, Modelling the influence of acoustic liner non-uniformities on duct modes, *Journal of Sound and Vibration* 219 (5) (1999) 859–879.
[5] A. McAlpine, M.C.M. Wright, Finite/boundary element assessment of a turbofan spliced intake liner at supersonic fan operating conditions, AIAA-2003-3305.
[6] J.H. Lan, C. Breard, Validation of 3D acoustic propagation code with analytical and experimental results, AIAA-2005-2901.
[7] D.M. Nark, F. Farassat, D.S. Pope, V. Vatsa, The development of the ducted fan noise propagation and radiation code CDUCT-LARC, AIAA-2003-3242.
[8] T. Elnady, H. Bodén, Hard strips in lined ducts, AIAA-2002-2444.
[9] J.S. Alonso, R.A. Burdisso, Sound radiation from the boundary in a circular lined duct with flow, AIAA-2003-3144.
[10] L.M.B.C. Campos, J.M.G.S. Oliveira, Optimization of circumferentially non-uniform acoustic liners in annular ducts, AIAA-2004-3034.
[11] B. Yang, T.Q. Wang, Y. Guan, An approach to predict ducted fan noise by boundary integral equation method, AIAA-2005-3068.
[12] M.H. Dunn, TBIEM3D—A Computer Program for Predicting Ducted Fan Engine Noise, NASA CR-97-206232.
[13] M.E. Goldstein, *Aeroacoustica*, McGraw-Hill International Book Company, 1976.